Research Article | Vol. 30, No. 12 / 6 Jun 2022 / Optics Express 21028

Optics EXPRESS

Influence of the thermodynamic properties of the Internal Occulter inside the coronagraph on coronal observations

JINCHENG WANG,[1,2] TAISHENG WANG,[1] CHENGYONG SHI,[1] MINGZHE SUN,[3] AND HONGXIN ZHANG[1,*]

[1] *R&D Center of Precision Instruments and Equipment, Changchun Institute of Optics, Fine Mechanics & Physics, Chinese Academy of Sciences, No. 3888, Dongnanhu Road, Changchun, Jilin 130033, China*
[2] *University of the Chinese Academy of Sciences, Beijing 100039, China*
[3] *Shandong Provincial Key Laboratory of Optical Astronomy and Solar-Terrestrial Environment, Institute of Space Sciences, Shandong University, No. 180, Wenhua West Road, Weihai, Shandong 264209, China*
[*] *firsthongxin@163.com*

Abstract: To detect good quality coronal spectra images, the continuous optimization of stray light suppression techniques for coronagraphs is required. The internal occulter (IO) serves as the main tool for the Internally Occulted Coronagraph to suppress the direct light from the photosphere layer, and thermal stress displacements with thermodynamic properties will overcover the information of the internal corona. In this paper, a reflective distribution function model is established according to Kirchhoff's principle which is based on a ground-based Lyot coronagraph, the aperture is 200 mm, detection wavelength is 637.4 nm (Fe X) and the work field range is ±1.05-2.0 R_S (R_S is the solar radius), thus the absorption rate is inverted. The irradiance at different positions received by the ground is simulated, and then the temperature change of the occulter during the time of the strongest radiation is calculated. The thermal stress displacement change of the two materials was analyzed by the finite element method. Comparison of the experiment shows that the displacement variation of the conical bottom plane results in losing 0.34% R_S corona information for the 2a12-t6 aluminum alloy, and losing 0.11% R_S coronal information for oxygen-free copper. This way provides a new idea for the thermodynamic modeling of the IO and the direct light suppression technology in the coronagraph.

1. Introduction

Corona-solar outer atmosphere, which contains rich physical processes, is an extremely important aspect in the physical study of Sun-Earth relations. The information plays a role in understanding issues such as coronal heating [1], solar wind acceleration mechanisms [2], and the origin of non-thermal particles [3]. Simultaneously, the solar corona is also a predominant source of perturbations that affect the Sun-Earth space environment, and changes in its environment often lead to drastic perturbations of the Earth's space environment so as to trigger catastrophic space weather [4,5], all these detection targets are continuously and dynamically monitored by coronagraphs for coronal mass ejections (CMEs) [6].

Since coronal imaging is affected by stray light from different sources, the target SNR is decreased and the coronal image is annihilated. The core task of the coronagraph is to suppress these stray lights. They can be classified into four levels from different sources [7], the first level is the direct light from the photosphere layer; the second level is the diffracted light from the objective stop, which is about 10^{-5}–10^{-6} $B_\odot$ ($B_\odot$ is the average brightness of the center of the heliopause); the third level is the ghost image of the secondary reflection from the inner surface of the objective, which is about 10^{-5} $B_\odot$; the fourth level is mainly the scattering caused by surface roughness, dust contaminants, impurities in the glass and material inhomogeneity

#459234 https://doi.org/10.1364/OE.459234
Journal © 2022 Received 27 Mar 2022; revised 27 Apr 2022; accepted 27 Apr 2022; published 26 May 2022

in the glass, which is less than 10^{-5} $B_{\odot}$. The coronagraph can be divided into three types according to direct light suppression forms, the first type contains the Seventh Orbiting Solar Observatory (OSO-7) [8], Large Angle and Spectrometric Coronagraph (LASCO) C2/C3 carried by Solar and Heliospheric Observatory (SOHO) [9]. The Solar Terrestrial Relations Observatory (STEREO) Cor1 [10] and Balloon-Borne Investigation of Temperature and Speed of Electrons in the Corona (BITSE) mission [11], jointly developed by NASA Goddard Space Flight Center and Korea Astronomy and Space Science Institute, have an external occulter structure. The second type, such as Lasco-Cor1 [9] and the Coronal Solar Magnetism Observatory (COSMO) K-coronagraph is one of three proposed instruments in the COSMO facility suite [12], both are internally occulted structures. The third type, such as the Sun Earth Connection Coronal and Heliospheric Investigation (SECCHI) [13], adopts the knife-edge side shield structure for large-field observation. To be closer to the active source region in ground-based observations, an inner-masked coronagraph is more suitable. The IO serves as the main carrier for suppressing direct light in the internal-occulted transmissive coronagraphs, the size of the occulter must be variable to account for the seasonal variation of the solar field of view size due to the solar-terrestrial distance and the variation of the effective focal length of the objective due to axial chromatic aberration [14]. Depending on the focusing characteristics of the objectives, it is known that the material and size of the IO will inevitably cause modifications in the thermodynamic properties of the occulter, and once the lateral displacement of the bottom surface of the occulter changes, it will definitely increase the loss of the inner field of view, which will have a great impact on the overall coronal observation, the localization of the active source area and the characterization of the scientific target.

The research relies on the Spectral Imaging Coronagraph (SIC) project of the Meridian Project II Solar-Interplanetary Supervision Chain (MEP II-SISC) detection program. The internal-occulted transmissive ground-based coronagraph will be placed at the Lijiang Observatory with an altitude of 3200 m. The field range is ±1.05-2.0 R_S. The ground-based coronagraphs currently observe high-temperature spectral lines (530.3 nm). This situation has a strong signal in the solar active region, however, the radiation signal in the coronal hole is very weak. The low-temperature spectral line Fe X (637.4 nm) is suitable for observing non-erupting coronal activities such as coronal holes. We can study the Alfvén waves propagating in different magnetic field structures, so we choose the central wavelength of 637.4 nm. The single point spectral imaging bandwidth is 1.2 Å. The objective focal length is 2000 mm and the aperture is 200 mm. The main work of this paper based on SIC is to design a series of IO that suppresses direct light over 5%. A reflective distribution function numerical model based on Kirchhoff's principle was developed, which can invert the absorption rate, the average received irradiance of the ground at different geographical locations was established that based on the principle of the solar photometer, The temperature variation of IO can be calculated from the law of energy conservation. Then a finite element analysis of IO in two different materials was carried out, and the temperature variation at the time of the strongest radiation has been compared with the experiment. Finally, the loss data of the internal corona information are obtained.

2. Fabrication of assembly

As the strongest non-essential source in coronagraphs, direct sunlight strongly affects the internal corona information of interest for ground-based observations. The theory to suppress direct light from the photosphere follows the general principle of the classical Lyot-style internally occulted coronagraph. a similar case in COSMO K-Cor [15] and STEREO-Cor1 [10] identified, the principle as shown in Fig. 1(a), it is known that κ is the focal plane of the objective and also the location of the field stop, and the radius is satisfied $r = f \times \tan\theta$, the value of f is focal length, θ is the field. However, considering the effect of edge diffraction and chromatic aberration, the over-occulting ratio of 5% is usually designed. As shown in Fig. 1(b), represents the fluctuation range of direct light maximum field and sun-earth distance in a year, while Fig. 1(c) calculates the size of haploid occulter radius and over-occulting radius. It is obvious that there is a change period from January to July every year, so only 7 groups of occulters need to be made through accurate calculation.

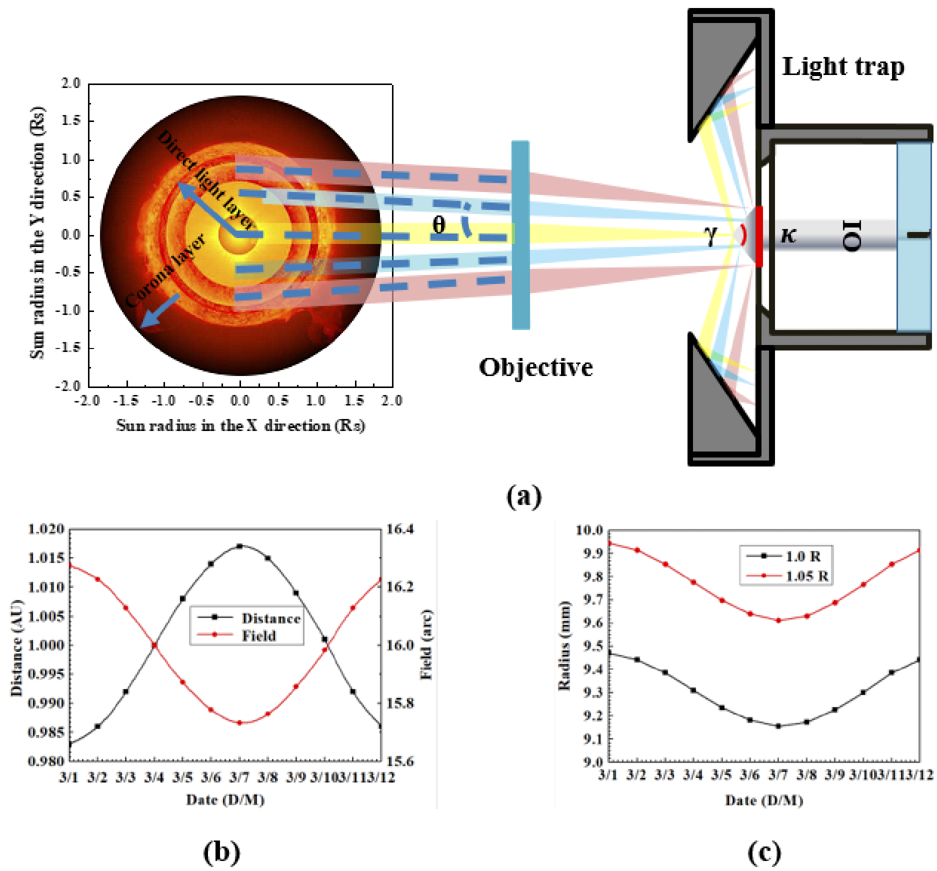

Fig. 1. Schematic diagram of the IO to suppress direct light. (a) the diagram of direct light being reflected into the light trap, (b) shows the periodic variation of the solar-terrestrial distance and the field of view during the year, (c) shows the maximum radius of the haploid occulter and the radius of 5% over-occulting.

In order to avoid the reflected light spilling out of the cone bottom into the subsequent light path, the occulter conical angle γ needs to be calculated precisely, as shown in Fig. 1(a). The light reflected will partially enter the back of plane κ when $\gamma \leq 90°$. We finally set the height of the cone as 6 mm, the γ will fluctuate between 115.5° (perihelion) and 117.2° (aphelion) that following $\gamma = 2\arctan h/R_I$.

The Lyot coronagraph adopts a perforated method to attach the field mirror, but the field mirror is broken during the processing. Another reason is that the objective as the primary mirror has no achromatic capability. The field lens can improve the ability of edge light to hit the detector, but also plays a crucial role in aberration correction. Therefore, the mechanical structure of the IO load device should also be optimally designed so that it does not affect the subsequent optical imaging, but also reduces the damage of the field lens.

As shown in Fig. 2, the schematic diagram of the overall mechanical structure of the IO mobile platform and the field lens, the three-dimensional schematic diagram of the IO translation stage

Optics EXPRESS

is composed of the IO, the field stop, the flat supporting the IO, the L-shaped load adjustable displacement platform, the bottom is the precision stepper motor of the displacement platform, which produces a focal shift at the focal plane of objective due to the wavelength switching from 530.3 nm to 637.4 nm, the distance is 16.79 mm backward, the wavelength of 530,3 nm is an alternative observation channel, in order to complement the high-temperature spectral data and obtain stokes parameters of the K corona, which also leaves room for modification for this study. Table 1 lists the main performance parameters of the precision stepper motor. The stroke is 20 mm, considering the light-weighting and stability, we choose aluminum alloy as the stepping motor material.

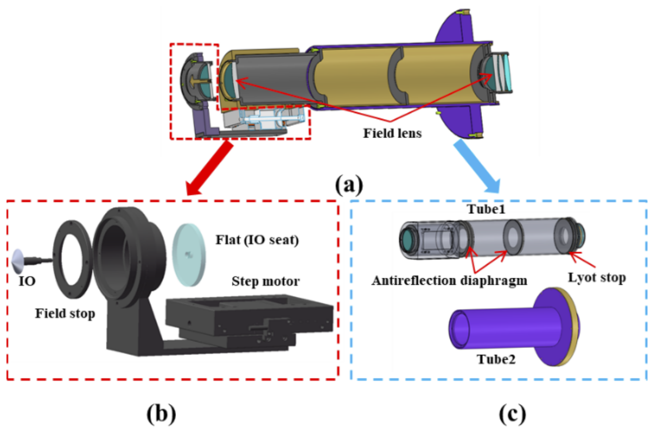

Fig. 2. Solid model of the IO and its supporting assembly, (a) cross-section drawn for the field lens and mechanical components, (b) is a diagram for bunkers and precision displacement stepper motor, (c) is a perspective view of the external tubes, back-end antireflection diaphragm and Lyot stop.

Table 1. The performance parameters of the precision stepper motor

Parameter	Value
External Power (V)	24
Stroke (mm)	20
Lead of the ball screw (mm)	0.62
Material	Aluminum alloy
Surface treatment	Anodic oxidation
Guide rails	Crossed roller guider
Maximum speed (mm/s)	5
Resolution (μm)	0.1 (With raster ruler)
Re-orientation accuracy (μm)	±0.2
Drive motor	28 linear pulse motors
Step angle	1.8°
Center load (kg)	5
Feedback signal	TTL
Location accuracy (μm)	±1
Control mode	Closed-loop
Change of focal length (mm)	16.79

The bottom surface and the support rod are black with absorbent material, the cone edge and cone top angle should be sharp, and the surface reflectivity should be high. The backend column part should ensure that it does not affect the imaging, through the calculation to get the support of the IO of the front surface of the flat sheet is located in the IO after 25 mm position, the length of the IO support rod preferably does not exceed 35 mm. The radius of the flat sheet opening and the support rod preferably does not exceed 6 mm, so as to avoid the introduction of new stray light from the coronal light shining on them. According to geometric optics, the field stop is generally placed in the same plane as the object image plane, and the radius of the field stop of our system is 19 mm.

3. Thermodynamic theoretical description

Due to the focusing of the lens, the accumulated heat is all concentrated on the IO surface in direct contact with direct sunlight. A first-order phase transition is generated internally under this premise, the IO surface is reflecting and absorbing energy at the same time, thermodynamic properties vary from different materials [16]. This property is analyzed in terms of its influence from the radiation point of view, and the maximum temperature change can be obtained by modeling the reflectance to invert the absorption rate. Finally, the loss of information on the internal corona is calculated from experimental combined with theoretical perspectives.

3.1. Inversion model of absorption rate

The ratio of monochromatic radiation emission to monochromatic absorption ratio is a universal function about frequency ν and temperature T, independent of the substance itself, which ignores the theoretical error caused by physical boundary conditions [17,18]. Subsequently, Kirchhoff proposed the law of thermal radiation in 1859, while any object emits radiant energy, it also continuously absorbs radiant energy from the surrounding environment. The difference between the energy radiated by an object and the energy absorbed is the net energy it transmits out. The radiant capacity of an object increases rapidly with increasing temperature. In general, when an object receives radiation from other objects, part of the radiation will be converted into heat, part of the radiation will be reflected, and part of the radiation will pass through the object. It can be seen from Kirchhoff's Law that the sum of the spectral absorbance α_λ, reflectance R_λ and transmittance T_λ is 1. Since the metallic material is opaque, thus $T_\lambda = 0$, the α_λ is inversely performed by modeling the reflectance. Figure 3 shows the schematic diagram of reflection distribution f_R. Rough surfaces can be regarded as numerous micro surfaces, and the amplitude of sin function can represent the surface undulation degree. The characteristic length L_c can accurately represent the surface undulation period, and L_c is correlated with surface roughness σ, so the influence of L_c and σ should be considered when describing R_λ.

Figure 3(a) shows the micro surfaces with two different roughness, the red arrows indicate the height from the top of the micro surface to the flat surface, the roughness is larger, i.e., the slope of the micro surface is larger, as shown in Fig. 3(a1), and the opposite in Fig. 3(a2). The red dashed box in Fig. 3(a) indicates the slope function of the micro surface, where Δl_I indicates the beam width in the incident direction, Δl_R is the beam width in the reflected direction, Δl indicates the surface slope length, and Δx indicates the horizontal length. According to Snell's law, the reflection area dA_R is equal to the incident area dA_I, i.e., $\Delta l_I = \Delta l_R$, and $\xi = \sqrt{\Delta l^2 - \Delta x^2}/\Delta x$. As shown in Fig. 3(b), the reflection on the micro surface will reflect the incident radiation in different directions in the hemispheric domain. The reflection function is expressed as:

$$f_R(\theta_R, \phi_R; \theta_I, \phi_I) = \frac{L_R(\theta_R, \phi_R, \theta_I, \phi_I)}{L_I(\theta_I, \phi_I)\cos\theta_I d\omega_I}, \tag{1}$$

The term (θ_I, ϕ_I) determines the direction of the incident light, (θ_R, ϕ_R) determines the direction of the reflected light, $d\omega$ indicates the micro-element stereo angle of the micro surface, L_I

Optics EXPRESS

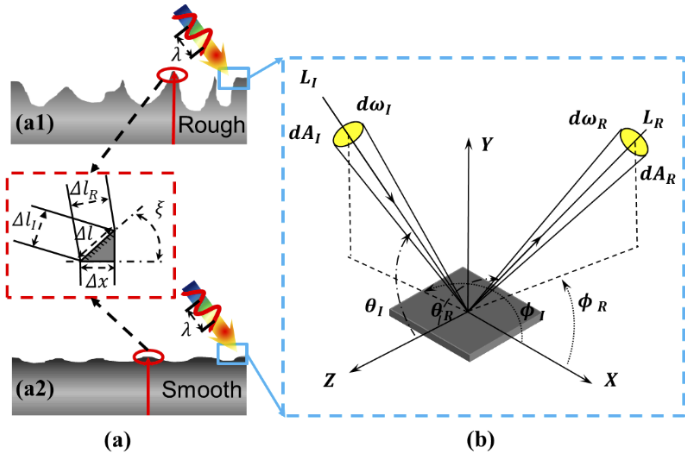

Fig. 3. The diagram of the micro surface slope function and the reflection distribution function. (a) shows the relation between light width and the metal micro surface, the (a1) shows the micro surface with large roughness, the (a2) shows the micro-surface with small roughness, the red dashed box indicates the slope function model, (b) shows the reflection distribution function f_R, which models the distribution of reflected radiation from the micro surface with the angle.

indicates the incident irradiance, and L_R indicates the reflected irradiance. Since micro surface dimensions are much larger than wavelengths, K. Tang [19] and J. Caron [20] obtained reflection distribution functions for p-polarized and s-polarized light in the direction of normal incidence based on the geometric optics assumption that:

$$\begin{aligned} f_{R,p} &= \frac{(\psi_s^2 \sin^2\phi_R + \psi_p^2 \cos^2\phi_R) p(\xi_x, \xi_y)}{4\cos\theta_R \cos^4\alpha}, \\ f_{R,s} &= \frac{(\psi_s^2 \cos^2\phi_R + \psi_p^2 \sin^2\phi_R) p(\xi_x, \xi_y)}{4\cos\theta_R \cos^4\alpha}, \end{aligned} \tag{2}$$

where ψ is the Fresnel coefficient, α is the micro surface inclination angle in the (θ_R, ϕ_R) direction with respect to the xoy plane, $p(\xi_x, \xi_y)$ is the slope function. But for any plane $\phi_R \neq 0°$, there are components in ψ that are both parallel and perpendicular to the plane. On the surface of an isotropic medium, $p(\xi_x, \xi_y)$ can be expressed as:

$$p(\xi_x, \xi_y) = \frac{1}{2\pi\xi_{rms}^2} \exp\left(-\frac{\xi_x^2 + \xi_y^2}{2\xi_{rms}^2}\right), \tag{3}$$

ξ_{rms} denotes the root mean square slope. Based on the Gaussian distribution function, $\xi_{rms} = \sqrt{2}\sigma/L_c$, and $L_c = V_{boday}/S_{area}$, When the incident direction $\theta_I \neq 0°$ and azimuth $\phi_I \neq 0°$, the ξ_x and ξ_y components in the slope function can be expressed as:

$$\begin{aligned} \xi_x &= -\frac{\sin\theta_I \cos\phi_I + \sin\theta_R \cos\phi_R}{1 + \cos\theta_R}, \\ \xi_y &= -\frac{\sin\theta_I \sin\phi_I + \sin\theta_R \sin\phi_R}{\cos\theta_I + \cos\theta_R}, \end{aligned} \tag{4}$$

At vertical incidence, $\theta_I = 0°$, $\phi_I = 0°$, thus $\xi_x = -\cos\theta_I/(\cos\theta_I + \cos\theta_R)$, $\xi_y = -\sin\theta_I/1 + \cos\theta_R$. $\beta = \tan^{-1}\xi_{rms}$ can be defined as the inclination angle of the micro surface. Since the radiation is

Optics EXPRESS

unpolarized, its reflection distribution function can be replaced by $f_R = (f_{R,p} + f_{R,s})/2$. Then the micro surface direction-hemispheric reflectance can be expressed as:

$$\rho_\lambda = \int_0^{2\pi} d\phi_R \int_0^{2\pi} f_R \sin\theta_R \cos\theta_R d\phi_R, \tag{5}$$

Figure 4 shows that $f_R \cos\theta_R$ in the case of $\xi_{rms} = 0.176$, $\beta = 10°$; $\xi_{rms} = 0.466$, $\beta = 25°$. It is obvious that $f_R \cos\theta_R$ is decreasing sharply and gradually to 0 when $\beta = 10°$. When $\beta = 25°$, the change of $f_R \cos\theta_R$ tends to be smooth, even if $\theta_R = 90°, f_R \cos\theta_R \neq 0$. This indicates that when the roughness is very small, with the increase of θ_R, the scattering phenomenon is not obvious in the range that the normal line as the center and the polar angle is relatively small. When the roughness is larger, $f_R \cos\theta_R$ changes slowly and the scattering phenomenon is obvious, and the radiation scattering phenomenon also occurs in larger polar angle range. The value of the factor at the intersection is equal, which implies that the scattering situation is the same at this point.

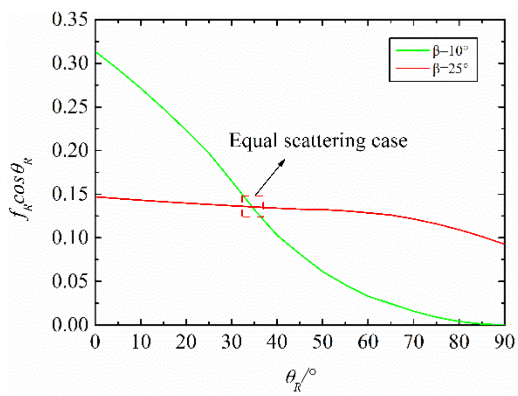

Fig. 4. the change of factor $f_R \cos\theta_R$ in the directional-hemispheric reflectance function.

Table 2 summarizes the influence of different roughness on normal emissivity ρ_λ, temperature error Δt on metal surfaces and the inversion results of absorptivity α_λ. where β corresponds to the relative values of 5.7μm, 11.5μm, 22.8μm, 28.5μm and 34.2μm respectively. Assuming that emissivity ($\rho = 0.7785$) is the standard value when roughness is 0. It can be concluded from Table 2 that β<20°, the temperature measurement error Δt<1°C; when $\beta = 25°$, Δt>2°C. The temperature error of IO is controlled within 2% when it was polished to a super smooth surface. Sensors are our key sensitive devices to reduce measurement errors, and with the maturity of modern processes, sensors can be classified as physical, chemical [21] and biological [22] sensors according to the type of measurement target. We use thermistor physical sensors for data acquisition, currently based on the AuNPs excitation of the local surface plasmon resonance (LSPR) principle of the sensor has a high sensitivity and sensor probe stability [2326], polymer optical fiber (POF) level sensors have compact structure and high coupling efficiency [27]. These sensors will help us to improve the measurement accuracy higher. But there is no actual product yet.

After reversing the absorptivity, according to the energy-specific heat capacity (E-SHC) law, the expressions for the ground received energy M_λ, the temperature change ΔT and the absorption rate α_λ can be related as:

$$M_\lambda = C \times \varphi \times V \times \Delta \times T = SP \times S \times \tau \times \alpha_\lambda, \tag{6}$$

C denotes the specific heat capacity of the object, φ is the density of the object, V is the volume of the object, S denotes the receiving area, τ denotes the receiving time and SP denotes

Table 2. Correlation between the temperature error, absorptivity and roughness

$\beta/°$	α_λ	ρ_λ	$\frac{\Delta\rho}{\rho}/‰$	$\Delta t/°C$
5	0.2198	0.7802	0. 218	0.04
10	0.2184	0.7816	0.398	0.28
20	0.2004	0.7996	2.710	0.85
25	0.1672	0.8328	6.974	2.38
30	0.1068	0.8932	14.737	6.25

the maximum solar irradiance in a day, it follows from the Beer-Bouguer-Lambert (BBL) law that can be expressed as [28]:

$$SP = SP_{\lambda,0}R^2 \exp[-m_s\tau_{total}(\lambda)], \tag{7}$$

where, R^2 is the sun-Earth correction coefficient, m_s is the solar atmospheric mass, in 1966, Kasten et al [29] proposed revised optical air quality tables and approximation formula:

$$m_s = \frac{1}{[\sinh + a \times (h+b)^{-c}]} \times \frac{p(z)}{p(0)}, \tag{8}$$

In which $p(0)$ is the standard atmospheric pressure of 101.325 kPa, h is the solar altitude angle, $p(z)$ is the atmospheric pressure at the observation point, a, b and c are constants. Where the solar altitude angle can be calculated by the following equation:

$$\sinh = \cos\partial_m \cos\delta \cos\Omega + \sin\partial_m \sin\delta, \tag{9}$$

∂_m is the latitude of the observation site, δ denotes the declination and Ω denotes the angle between the hour circle where the sun is located and the astronomical meridian circle of the observation site, thus $-90° \le h \le 90°$. The atmospheric masses was shown in Fig. 5 are obtained from the solar irradiance (SP = 20.89254 W/m^2) outside the atmospheric boundary given by the Commission for Instruments and Methods of Observations (CIMO) [30], and the corrected values a = 0.50572, b = 6.07995, c = 1.6364 given by the ISO Standard. The ground received solar irradiance at the observation site and the experimental site as shown in Fig. 6.

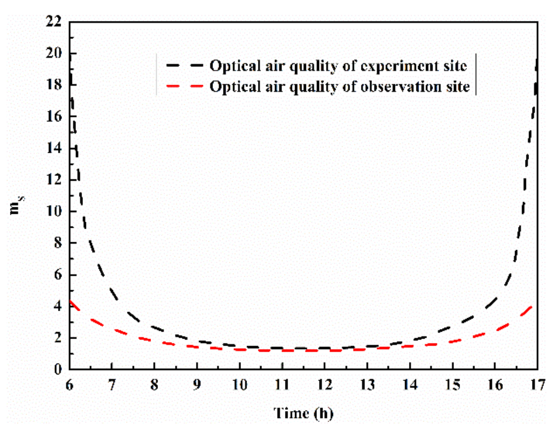

Fig. 5. Air quality model of observation site and experiment site, the air quality is equal at around 12:00.

As shown in Fig. 6, $\overline{SP}$ is the mean value of the strongest radiation reception time period, the mean irradiance of the observation site is 16.2 W/m^2 and the experimental site is 13.8 W/m^2.

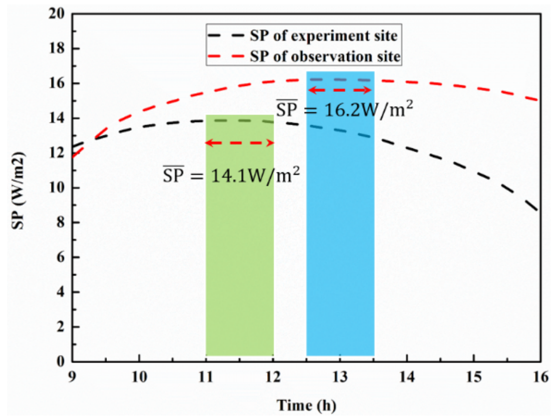

Fig. 6. Ground received irradiance model at the observation and test sites.

The final calculation of the maximum temperature amplitude with 2a12-t6 aluminum alloy as the material is $\Delta T_{Al} = 83.17°C$, and $\Delta T_{cu} = 65.25°C$ when oxygen-free copper is the material.

3.2. Thermal stress displacement

Depletion of the observed field by the IO belongs to the influence mechanism of the Planar Axisymmetric Temperature Field-Stress Displacement (PATF-SD). The bottom surface of the IO is defined as the *xoy* plane, and the expression of the stress displacement component from the finite element perspective as below:

$$\begin{aligned} \varepsilon_x &= \frac{1}{E}(\sigma_x - \nu\sigma_y) + \eta T, \\ \varepsilon_y &= \frac{1}{E}(\sigma_y - \nu\sigma_x) + \eta T, \end{aligned} \tag{10}$$

where E denotes Young's modulus, ν denotes Poisson's ratio, σ_x and σ_y denote the stress tensor in the directions of x and y, η denotes the coefficient of thermal expansion, the value of mechanical parameters are shown in Table 3. In the case of solid stress, $1/E(\sigma_y - \nu\sigma_x) \ll \eta T$, assuming that the strain is linear with temperature and causes only positive strain but not shear strain, i.e., $\varepsilon = \eta T$, and the material is isotropic, then $\varepsilon_x = \varepsilon_y$.

Table 3. Mechanical parameters of the material

	2a12-t6 aluminum alloy	Oxygen-free copper
Young's modulus (Gpa)	68	115
Poisson's ratio	0.3	0.34
Density (g/m3)	2.8	8.94
Conductivity (W/m.K)	220	391

From Fig. 7, we can see that stress is different for IO made by different materials, as shown in Fig. 7(a), the maximum light heating power at the bottom edge of the shelter is $p_i = 4.54 \times 10^6$ W/m^2, Fig. 7(b) represents the single point thermal stress $F_{Al} = 4.43 \times 10^6$ N/m^2 at the edge of aluminum alloy, Fig. 7(c) represents the single point thermal stress $F_{Cu} = 2.19 \times 10^6$ N/m^2 at the edge of copper alloy.

We can see from Fig. 8(a) and (b) that the maximum temperature is $101.1°C$ for aluminum alloy and $86.0°C$ for copper alloy, the result is in accordance with the theory. Figure 8(c) shows

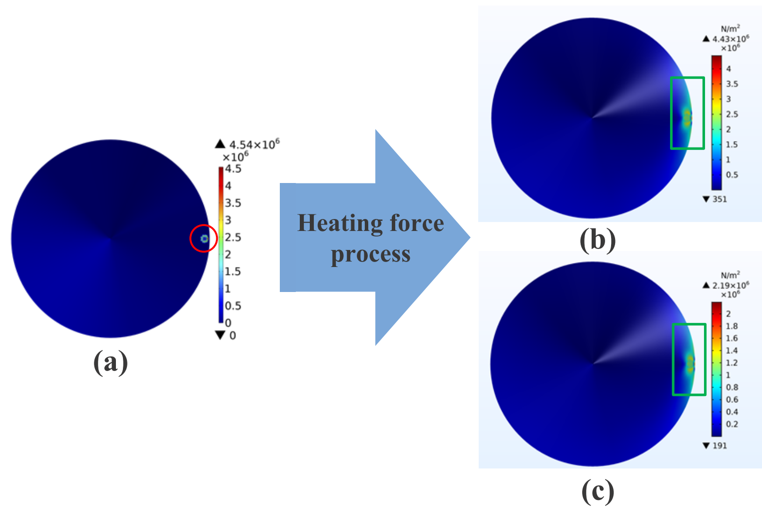

Fig. 7. The maximum light heating power and the stress for IO at the bottom edge, (a) shows the Light heating change process, (b) shows the stress for aluminum alloy, (c) the stress for copper alloy.

the trend of temperature change over time. Subsequently, we know the coefficient of thermal expansion is $2.20 \times 10^{-5}/{}^{\circ}C$ for aluminum alloy, and the coefficient of thermal expansion is $1.75 \times 10^{-5}/{}^{\circ}C$ for copper alloy. The displacement of aluminum alloy is 36.36μm, copper alloy is 21.61μm.

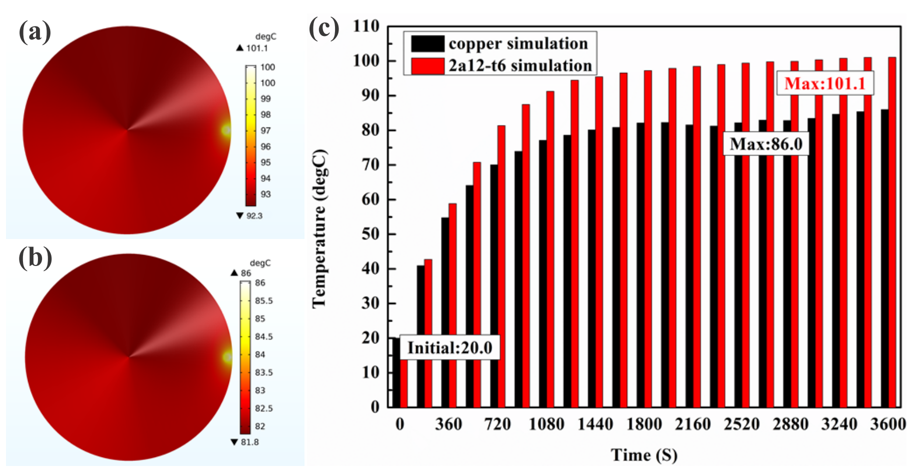

Fig. 8. The steady state and transient state. (a) Transient state diagram of the aluminum alloy. (b) Transient state diagram of the copper alloy. (c) Transient state diagram of the temperature trend.

In order to simulate the results with high accuracy, this is important to see the contribution of the objective to the effect of the results that under the longtime cumulative effect of the full sun radiation. Although the objective is directly exposed to direct light, the surface temperature of the Corning 7980 material has a small temperature variation only about $3^{\circ}C$ due to the stability and high transmittance. As shown in Fig. 9(a), the heating power is uniform, from the Fig. 9(b) and Fig. 9(c), we can notice the temperature variation gradually increases from outside to inside, the

Fig. 9(d) shows that the gradient of refractive index is 3.5×10^{-5}, Fig. 9(e) is the stress changing synchronously with temperature. Finally, we know the displacement of the objective is 0.12μm from the Fig. 9(f).

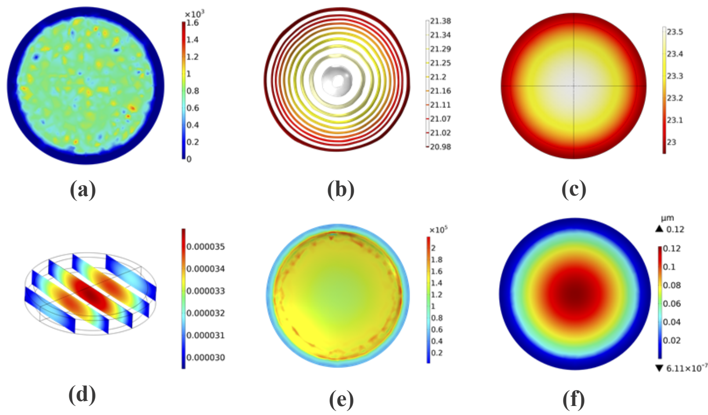

Fig. 9. The Schematic diagram of the characteristic parameters about the objective. (a) The heating power on the objective, (b) shows the isotherm, (c) shows the temperature variation of the objective, (d) shows the index variation, (e) shows the stress of the objective, (f) shows the displacement.

4. Experiment result and discussion

As shown in Fig. 10(a), to verify the correctness of the theory, the experimental platform was designed, Fig. 10(b) and (b) were the actual situation of the IO. The results were obtained after continuous observation for 1 hour, as shown in Fig. 10(c) and (e).

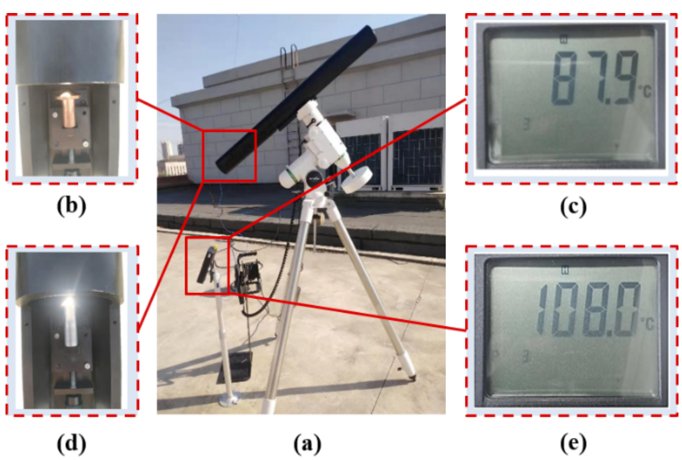

Fig. 10. The equipment to detect the temperature of IO. (a) Shows the device, (b) the copper IO in the field test, (c) the final temperature of the copper IO, (d) the aluminum IO in the field test, (e) the final temperature of the aluminum IO.

Figure 11 shows that the experimental results of the two materials are in good agreement with the theory, and the errors are within a reasonable range, the line graph is the change in temperature, the bar graph is the error of simulation and experiment. When the temperature rises near the maximum value, the errors are relatively stable and fluctuate greatly at the beginning of temperature rise, indicating that the molecules inside the materials are more active at the beginning of temperature rise.

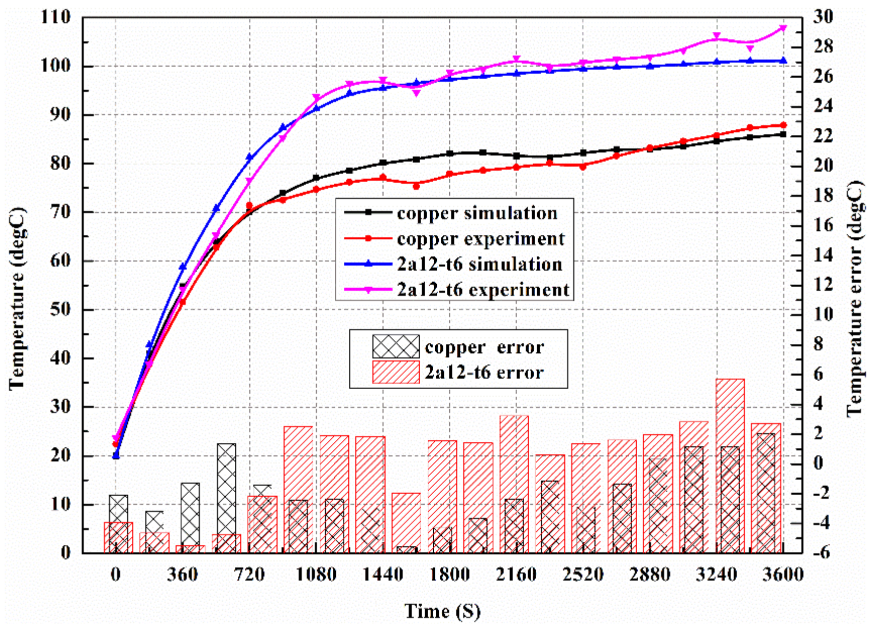

Fig. 11. Comparison between experiment and simulation.

In order to verify the impact of the experiment on the observation, we heated the bottom of the IO at the same temperature with a floor heater in the laboratory, as shown in Fig. 12. The bottom is offset from the original position to different degrees. r_0 is the original radius, r_1 is the radius after the change of aluminum, and r_2 is the radius after the change of copper, so $r_1 > r_2 > r_0$, then moving the IO into the optical path quickly, as shown in Fig. 13, O1 is the objective, O2 is the field lens, and O3 is the relay lens, The yellow solid line indicates that the ghost image is absorbed at the Lyot spot, and the black dotted line indicates that the diffraction light of the aperture stop is blocked by the Lyot stop, finally the coronal light reaches the CCD. We use the simulation source to do this work, in order to see the obvious phenomenon, where the minor direct light is allowed to leak past the edge of the IO.

Imaging results are obtained through experiments as shown in Fig. 14. Since the laser is not an ideal Lambert-type source, the brighter part is not a uniform ring. From Fig. 13(a) and Fig. 14(b), it can be obviously observed that the direct light overpasses the IO. As shown in Fig. 14(b), we can see that the effect of the image obtained after the experiment with oxygen-free copper is weaker than the experiment with aluminum alloy. Then the gray value variation is shown in Fig. 15. The parts with higher gray values almost overlap

Different materials with different internal structural factors will produce different 2D phase transitions under the same environmental variable conditions [31]. Simultaneously, for these two materials we have fully discovered their impact on coronal observations. In solar physics, the dynamization process of the delicate corona is an important category, so errors caused by non-essential external factors still need to be considered carefully.

Optics EXPRESS

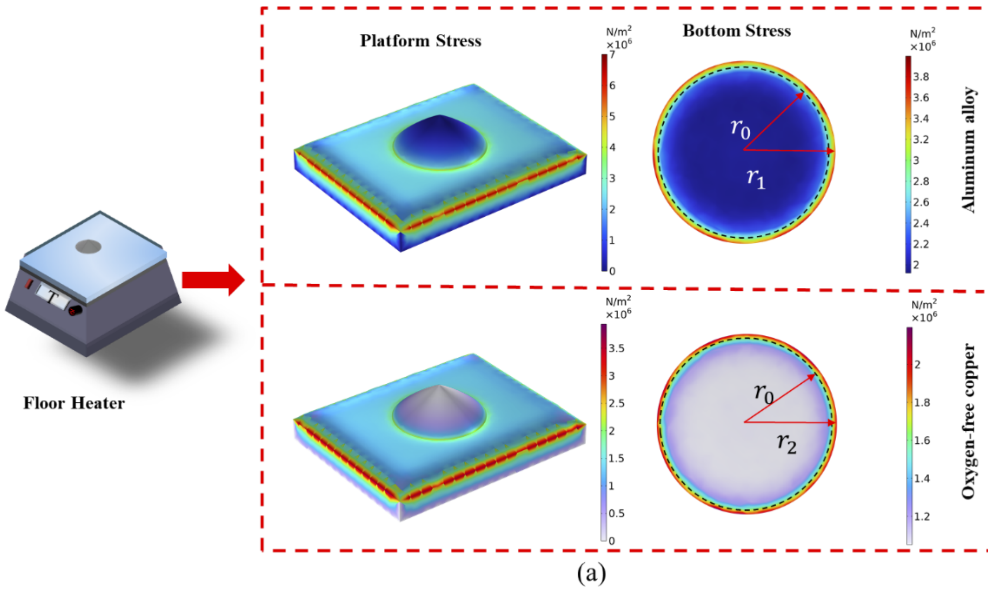

Fig. 12. The diagram of the floor heater and the variation of the bottom.

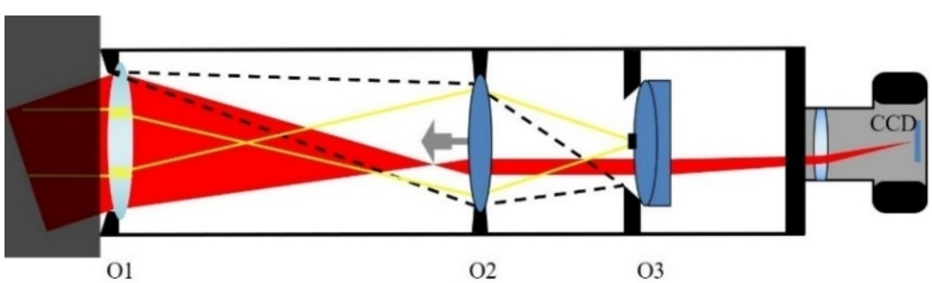

Fig. 13. The schematic diagram of Lyot coronagraph.

Optics EXPRESS

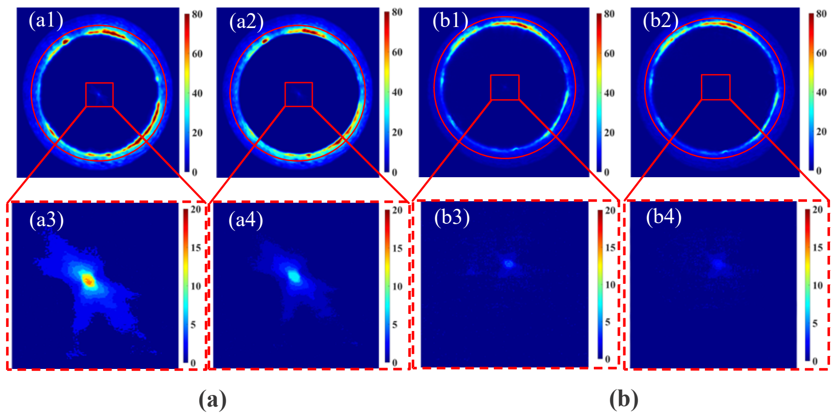

Fig. 14. Original images and Hot images. (a) is an image of the experiment taken using an IO made by aluminum alloy, (a1) shows the original picture, (a2) shows the hot picture, (a3) is the origin detail after enlargement, (a4) is the hot detail after enlargement. (b) is an image of the experiment taken using an IO made by Oxygen-free copper, (b1) shows the original picture, (b2) shows the hot picture, (b3) is the origin detail after enlargement, (b4) is the hot detail after enlargement.

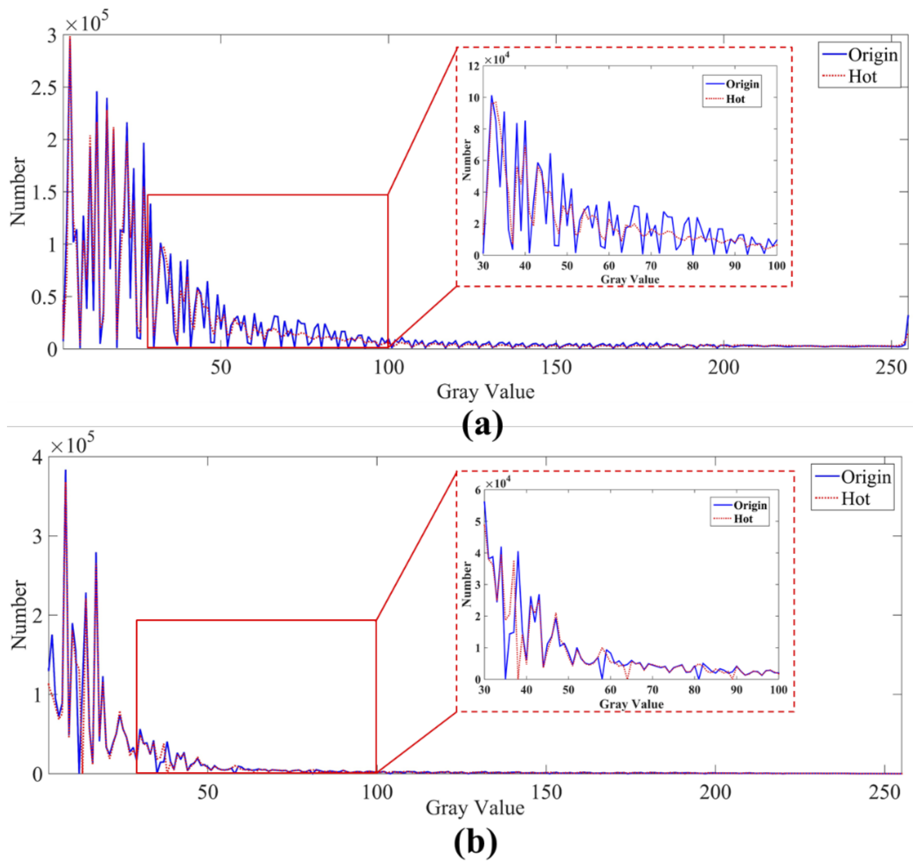

Fig. 15. The gray value of the original images and heated images, (a) shows the gray value comparison of aluminum IO, (b) shows the gray value comparison of copper IO. Data with pixel values in the 30-100 range has been locally magnified.

5. Conclusions

The internal occulter is an important strategy to suppress direct light in corona observation, this paper mainly conducts reflection distribution function modeling and finite element analysis on the IO made of two kinds of materials, and finally proves the rationality of the algorithm through experiments. For the IO made of aluminum alloy, after being heated by the full spectrum of solar rays, the shape variation will reach 0.18% of the original diameter, and the field of view will be lost about 0.34% of the solar radius, i.e., if the coronal observation is conducted above the relative chromosphere, the coronal information of 4729.4 km will be lost. The maximum deformation of the copper alloy diameter is only 0.11% of the original diameter, and the field of view will be lost about 0.18% of the solar radius, the coronal information of 2503.8 km will be lost. This model analyzes the influence from different perspectives and provides a technology for the optimization of the IO material. But the selection of materials is limited for us. In future studies, we will analyze the IO of other materials, the purpose is to provide data for the design and material selection of the IO at different observation sites.

Funding. National Natural Science Foundation of China (41627806); Strategic Pioneering Science and Technology Special Project of Chinese Academy of Sciences (XDA15018502); Civilian Space Technology Advance Research Project (D030203).

Disclosures. The authors declare that there are no conflicts of interest related to this paper.

Data availability. Data underlying the results presented in this paper are not publicly available at this time but maybe obtained from the authors upon reasonable request.

References

1. R. Walsh and J. Ireland, "The heating of the solar corona," Astron. Astrophys. Rev. **12**(1), 1–41 (2003).
2. C. Chen, B. Chandran, L. Woodham, S. Jones, J. Perez, S. Bourouaine, T. Bowen, K. Klein, M. Moncuquet, and J. Kasper, "The near-Sun streamer belt solar wind: turbulence and solar wind acceleration," Astron. Astrophys. **650**, L3 (2021). special issue on Solar Wind.
3. K. Mori, C. Hailey, G. Bridges, S. Mandel, A. Garvin, B. Grefenstette, W. Dunn, B. J. Hord, G. Branduardi-Raymont, and J. Clarke, "Observation and origin of non-thermal hard X-rays from Jupiter," Nat. Astron. (to be published).
4. C. Kay, M. L. Mays, and Y. M. Collado-Vega, "OSPREI: A Coupled Approach to Modeling CME-Driven Space Weather with Automatically-Generated, User-Friendly Outputs," Space Weather. (to be published).
5. C. N. S. Resonances, "Schumann Resonances, a plausible biophysical mechanism for the human health effects of Solar/Geomagnetic Activity," Nat. Hazards (Dordr) **26**(3), 279–331 (2002).
6. S. Kahler, "Coronal mass ejections," Rev. Geophys. **25**(3), 663–675 (1987).
7. B. Lyot, "The study of the solar corona and prominences without eclipses (George Darwin Lecture, 1939)," Mon. Notices Royal Astron. Soc. **99**(8), 580–594 (1939).
8. S. Koutchmy, "Space-borne coronagraphy," Space Sci. Rev. **47**(1-2), 95–143 (1988).
9. G. Brueckner, R. Howard, M. Koomen, C. Korendyke, D. Michels, J. Moses, D. Socker, K. Dere, P. Lamy, and A. Llebaria, "The large angle spectroscopic coronagraph (LASCO)," Sol. Phys. **162**(1-2), 357–402 (1995).
10. R. A. Howard, J. Moses, A. Vourlidas, J. Newmark, D. G. Socker, S. P. Plunkett, C. M. Korendyke, J. Cook, A. Hurley, and J. Davila, "Sun Earth connection coronal and heliospheric investigation (SECCHI)," Space Sci. Rev. **136**(1-4), 67–115 (2008).
11. N. Gopalswamy, J. Newmark, S. Yashiro, P. Mäkelä, N. Reginald, N. Thakur, Q. Gong, Y.-H. Kim, K.-S. Cho, and S.-H. Choi, "The Balloon-Borne investigation of temperature and speed of electrons in the corona (BITSE): mission description and preliminary results," Sol. Phys. **296**(1), 15–32 (2021).
12. D. Gallagher, S. Tomczyk, H. Zhang, and P. G. Nelson, "Optical design of the COSMO large coronagraph," Proc. SPIE **8444**, 84443P (2012).
13. R. Harrison, C. Davis, and C. Eyles, "The STEREO heliospheric imager: how to detect CMEs in the heliosphere," Adv. Space Res. **36**(8), 1512–1523 (2005).
14. D. G. Socker, R. A. Howard, C. M. Korendyke, G. M. Simnett, and D. F. Webb, "NASA Solar Terrestrial Relations Observatory (STEREO) mission heliospheric imager," Proc. SPIE **4139**, 284–293 (2000).
15. D. Gallagher, Z. Wu, B. Larson, P. G. Nelson, P. Oakley, S. Sewell, and S. Tomczyk, "The COSMO coronagraph optical design and stray light analysis," Proc. SPIE **9906**, 990654 (2016).
16. B. Linder, *Thermodynamics and introductory statistical mechanics*, 1st ed. (John Wiley & Sons, 2004).
17. R. M. Goody and Y. L. Yung, *Atmospheric radiation: theoretical basis*, 2nd ed. (Oxford university press, 1995).
18. X. Yang and B. Wei, "Exact research on the theory of the blackbody thermal radiation," Sci. Rep. **6**(1), 1–5 (2016).
19. K. Tang and R. O. Buckius, "A statistical model of wave scattering from random rough surfaces," Int. J. Heat Mass Transfer **44**(21), 4059–4073 (2001).

20. J. Caron, J. Lafait, and C. Andraud, "Catastrophe theory interpretation of multiple peaks produced by light scattering from very rough dielectric surfaces," Phys. B **325**, 76–85 (2003).
21. Y. Wang, G. Zhu, M. Li, R. Singh, C. Marques, R. Min, B. K. Kaushik, B. Zhang, R. Jha, and S. Kumar, "Water Pollutants p-Cresol Detection Based on Au-ZnO Nanoparticles Modified Tapered Optical Fiber," IEEE Trans. Nanobiosci. **20**(3), 377–384 (2021).
22. G. Zhu, Y. Wang, Z. Wang, R. Singh, C. Marques, Q. Wu, B. K. Kaushik, R. Jha, B. Zhang, and S. Kumar, "Localized Plasmon-Based Multicore Fiber Biosensor for Acetylcholine Detection," IEEE Trans. Instrum. Meas. **71**, 1–9 (2022).
23. S. Kumar, Z. Guo, R. Singh, Q. Wang, B. Zhang, S. Cheng, F.-Z. Liu, C. Marques, B. K. Kaushik, and R. Jha, "MoS_2 Functionalized Multicore Fiber Probes for Selective Detection of Shigella Bacteria Based on Localized Plasmon," J. Lightwave Technol. **39**(12), 4069–4081 (2021).
24. M. Li, R. Singh, C. Marques, B. Zhang, and S. Kumar, "2D material assisted SMF-MCF-MMF-SMF based LSPR sensor for creatinine detection," Opt. Express **29**(23), 38150–38167 (2021).
25. M. Li, R. Singh, M. S. Soares, C. Marques, B. Zhang, and S. Kumar, "Convex fiber-tapered seven core fiber-convex fiber (CTC) structure-based biosensor for creatinine detection in aquaculture," Opt. Express **30**(8), 13898–13914 (2022).
26. Z. Wang, R. Singh, C. Marques, R. Jha, B. Zhang, and S. Kumar, "Taper-in-taper fiber structure-based LSPR sensor for alanine aminotransferase detection," Opt. Express **29**(26), 43793–43810 (2021).
27. R. He, C. Teng, S. Kumar, C. Marques, and R. Min, "Polymer Optical Fiber Liquid Level Sensor: A Review," IEEE Sens. J. **22**(2), 1081–1091 (2022).
28. T. G. Mayerhöfer, S. Pahlow, and J. Popp, "The Bouguer-Beer-Lambert law: Shining light on the obscure," ChemPhysChem **21**(18), 2029–2046 (2020).
29. F. Kasten and A. T. Young, "Revised optical air mass tables and approximation formula," Appl. Opt. **28**(22), 4735–4738 (1989).
30. F. Kasten, "A new table and approximation formula for the relative optial air mass," Arch. Meteorol., Geophys. Bioklimatol., Ser. B **14**(2), 206–223 (1965).
31. W. Li, X. Qian, and J. Li, "Phase transitions in 2D materials," Nat. Rev. Mater. **6**(9), 829–846 (2021).